Instrumentation sensitivities for tower-based solar-induced fluorescence measurements

Julia K. Marrs [a,*,1], Taylor S. Jones [a,1], David W. Allen [b,2], Lucy R. Hutyra [a,1]

[a] *Department of Earth & Environment, Boston University, 675 Commonwealth Avenue, Rm. 130, Boston, MA 02215, USA*
[b] *Remote Sensing Group, National Institute of Standards and Technology, 100 Bureau Drive, Gaithersburg, MD, 20899, USA*

ARTICLE INFO

ABSTRACT

Solar-induced chlorophyll fluorescence (SIF) has been widely cited as a proxy for photosynthesis and is being incorporated as a common input in terrestrial primary productivity models. Though satellite-based SIF products show close relationships with terrestrial gross primary productivity (GPP), there is wide variability in the magnitude of published SIF retrievals made at intermediate scales. In a meta-analysis of the tower-based and airborne SIF literature, we found that mean SIF retrievals from unstressed vegetation spanned a wide range, from 0.041 mW m^{-2} nm^{-1} sr^{-1} to 14.8 mW m^{-2} nm^{-1} sr^{-1}, with a majority of values falling below 4 mW m^{-2} nm^{-1} sr^{-1}. We compiled information on reported spectrometer calibration procedures, hardware characterizations, and associated corrections from these same papers, and found inconsistent reporting on if and how key calibration methodology was performed. In order to quantify the importance of such methodological differences on final SIF retrievals made at a proximal scale, we performed radiometric calibrations and corrections for electronic dark current, detector noise, atmospheric O_2 absorbance, and cosine corrector effects on three field-deployed spectrometers. We found dramatic changes in SIF retrieval magnitude before and after applying calibrations and corrections, as well as significant differences between instrument performance in the field and expected performance based on laboratory characterizations. Based on these tests, and on a Monte Carlo simulation of uncertainty estimates associated with each of these corrections, it is likely that calibration methodologies and hardware characterizations explain some of the observed variability in published SIF retrievals. This wide range in baseline SIF retrieval methodologies and resultant magnitudes severely limit researchers' ability to synthesize and advance the utility of SIF in modeling GPP across scales. Further, variability in calibration and correction methodology may explain the weak SIF-GPP relationship across studies at tower scales.

1. Introduction

The terrestrial biosphere is a crucial sink for anthropogenic emissions of carbon to the atmosphere (Pan et al., 2011), but is also the source of the largest uncertainties in estimated global carbon budgets (Le Quéré et al., 2018). These uncertainties arise in part because global models of the gross primary productivity (GPP) of vegetation are limited by insufficient data to fully constrain outputs (Anav et al., 2015) and by underlying assumptions that oversimplify real-world heterogeneity. Long-running satellite programs have persistently monitored global vegetation via greenness indices (Thompson et al., 2017), but these also suffer limitations associated with saturation at moderately high leaf area

(Asner et al., 2004). As a potentially more direct measure of GPP, there has been increasing interest in measuring solar-induced fluorescence (SIF) (Ryu et al., 2019), a faint chlorophyll fluorescence signal originating from the dissipation of excess light absorbed by plants (e.g. Krause and Weis, 1991). If more energy is absorbed by a leaf than can be used for photosynthesis on an instantaneous basis, plants may re-radiate light at a longer wavelength as one of several strategies to dissipate this unused energy and avoid cellular damage (e.g. Baker, 2008; Porcar-Castell et al., 2014).

Recent advances in remotely measuring GPP take advantage of this signal as a means of remotely tracking primary productivity. Satellite platforms measure solar-induced fluorescence (SIF) as a weak

* Corresponding author.
  E-mail addresses: jmarrs@bu.edu (J.K. Marrs), tsjones@bu.edu (T.S. Jones), david.allen@nist.gov (D.W. Allen), lrhutyra@bu.edu (L.R. Hutyra).
[1] 675 Commonwealth Avenue, Boston, MA 02215, USA.
[2] 100 Bureau Drive, Gaithersburg, MD 20899, USA.

enhancement in the apparent reflectance inside solar Fraunhofer lines and atmospheric absorption features (Meroni et al., 2009). SIF shows a strong linear relationship with GPP at the satellite scale (Frankenberg et al., 2011; Sun et al., 2018; Verma et al., 2017). However, the near-universal correlation reported between satellite SIF and flux tower estimates of GPP (Li et al., 2018b; Xiao et al., 2019) may be driven by satellite view angle (Zhang et al., 2018), canopy structure (Dechant et al., 2020) and temporal aggregation or averaging (Lin et al., 2019), independent of a physiological link. In general, averaging over areas of vegetation with heterogeneous physiological states likely linearizes the satellite SIF-GPP relationship to a greater degree than would be observed at the leaf level (Gu et al., 2019a). While the relationship between GPP and SIF is also encouraging at tower and airborne scales (Magney et al., 2019a; Yang et al., 2017; Zarco-Tejada et al., 2016), the link between SIF measured from a remote platform and plant physiology on the ground remains a crucial area of study.

Previous work confronting these challenges has employed intermediate-scale measurements from towers, drones, or light aircraft, which offer the opportunity for closer comparisons with flux tower and leaf-level quantifications of primary productivity. There is some evidence that the SIF-GPP relationship may hold across spatial and temporal scales (Duveiller and Cescatti, 2016; Wieneke et al., 2018; Wood et al., 2017) and that more nuanced relationships observed at finer spatiotemporal scales may not contradict linear relationships found elsewhere (Magney et al., 2020). Nonetheless, other authors show that intermediate-scale SIF measurements are subject to diurnal (Campbell et al., 2019; Middleton et al., 2017), seasonal (Liu et al., 2017; Nichol et al., 2019), and structural (Goulas et al., 2017; Migliavacca et al., 2017) effects that influence attempts to directly relate these values to GPP. Additionally, the interpretation of SIF values measured from towers and aircraft is complicated by the variety of associated instrumentation and measurement geometries. There are substantial uncertainties around absolute SIF retrieval magnitude associated with differences in spectral resolution (Julitta et al., 2016), changes in ambient temperature (Li et al., 2018a), atmospheric conditions along the viewing path to vegetated targets (Sabater et al., 2018), sensor noise (Burkart et al., 2015), stray light effects (Albert et al., 2019), SIF retrieval method (Chang et al., 2020), and the calibration and characterization of deployed hardware. Various methods for accounting for each of these potential error sources have been considered (Gu et al., 2019b) and their influence on final SIF retrievals quantified within individual field-deployed systems (Frankenberg et al., 2018; Grossmann et al., 2018). While each of these factors may individually contribute only a small amount of error, these uncertainties compound when attempting to retrieve a dynamic fluorescence signal that counts for only 1% to 5% of incoming radiance (Meroni et al., 2009). Recent work by Pacheco-Labrador et al. (2019) modeled the effects of numerous potential sources of uncertainty originating from typical SIF-measuring instrumentation and hardware. In this work, we sought to investigate how these crucial factors have been taken into account in the published literature, and to expand upon this comprehensive characterization of error sources by investigating the effects of instrument deployment in a field setting.

We performed a meta-analysis of SIF values and retrieval methods, target type, vegetation stress conditions, hardware specifications, and calibration methodology. We contextualized calibrations and hardware characterizations in our field-based system within the published literature on tower-based and airborne SIF retrievals. That literature stretches back nearly two decades and includes a wide variety of measurement platforms deployed across seasons and land cover types for a variety of purposes. In order to understand and correct for these same effects on a field-deployed system, we performed a variety of calibrations and characterizations in both laboratory and field settings. Using those data, we analyzed the effects of these factors on the magnitude of, and uncertainty around, retrieved SIF values. Using these two complementary analyses, we examined sources of hardware-based and environmental

uncertainty that may contribute to variability in SIF retrieval magnitude and SIF-GPP relationships at intermediate scales.

2. Methodology

2.1. Meta-analysis

In order to capture information on SIF values observed at the tower scale, we performed a meta-analysis of the published literature. On 19 September 2019, a Web of Science search was performed using the search terms "sun induced fluorescence" OR "solar induced fluorescence" AND "tower" (capitalized conjunctions indicate search engine logical operators). The search was repeated with the term "airborne" in place of "tower," but this search yielded an identical list. Our search returned 246 papers, and an initial check was performed by scanning abstracts and methods sections for mentions of SIF data collected from tower, drone, crane, or airborne platforms. Studies of only data from satellite-based platforms or which concerned only modeling work with no field component were excluded from this analysis. This resulted in a final pool of 61 papers published since 2003, which were then examined in depth. Details were extracted on numerous variables, including maximum and mean SIF values for control and (if applicable) stress conditions, instrument specifications, target vegetation location and species, data collection protocol, SIF retrieval method, and whether and how a variety of calibrations and corrections were performed. Calibrations and corrections investigated included those that introduce random error, such as stray light and detector signal-to-noise ratio, those that can introduce constant offsets, such as the choice of a radiometric light source for calibration, those that are dependent on sun angle and illumination level, such as detector nonlinearity, correction for electronic dark signal, or choice of cosine corrector material, as well as distance-dependent effects of atmospheric corrections. A plot visualizing the number of corrections applied by the papers in this analysis can be found in supplemental information (SI) Fig. 1a. Data were recorded for a total of 56 variables; the full results of this meta-analysis can be found in SI Table 1. A majority, 57 papers, reported SIF data in radiometric units, rather than as uncalibrated digital numbers, or relative quantifications of fluorescence magnitude. Of these, 23 also reported data on GPP, gross ecosystem productivity (GEP), or leaf-level net carbon assimilation (A_{net}) on the same vegetation targets from which SIF data were collected.

Maximum and mean values of SIF and primary productivity were taken directly from the publication when possible, or were extracted as hand-digitized points from relevant figures using Plot Digitizer software (Huwaldt, 2015). All available points from relevant figures were digitized, sometimes including those representing variable sky conditions or low-light hours. However, many authors specified that their reported data were filtered for the influence of clouds or otherwise subsetted to include only SIF retrievals made in high-light conditions; no paper represented in this meta-analysis presented data from exclusively low-light conditions. Because of differences in scope across all the papers in this analysis, the mean values in SI Table 1 represent averages over different time scales. Details of these differences in temporal scale are noted in the table, but were not analyzed in detail here.

2.2. Study site

Field measurements were made at the Forested Optical Reference for Evaluating Sensor Technology (FOREST) test site, established in 2016 on the campus of the National Institute of Standards and Technology (NIST) as a testbed for urban carbon monitoring alongside instrument calibration and validation procedures (Marrs et al., 2020). The FOREST site is a remnant stand of large-stature forest (~165 Mg C ha^{-1}) dominated by oaks and tulip poplars. Within a one hectare plot, biometric and environmental parameters, including soil temperature, soil moisture, air temperature, relative humidity, stem respiration, soil respiration, sap flux, and atmospheric CO_2 concentration were measured at frequent

intervals as detailed in Smith et al. (2019). Complementary atmospheric measurements from a nearby weather station on the NIST campus further facilitated the examination of links between observable optical signals and underlying biophysical phenomena.

2.3. Laboratory calibration and characterization

Three Ocean Insight QE Pro grating spectrometers (Ocean Insight, Largo, FL, USA)[3] were characterized during the process of testing and deploying field instrumentation. Over the course of the 2017–2019 summer field seasons, the same spectrometer (QE Pro 1) was used to measure reflected radiance and fluorescence from vegetated targets. One spectrometer (QE Pro 2) was used to measure downwelling solar irradiance during the 2017 season, and was replaced with QE Pro 3 for the 2018 and 2019 field seasons. All field SIF retrievals presented here were collected with a dual-spectrometer setup, where QE Pro 1 collected reflected radiance and fluorescence, and either QE Pro 2 or QE Pro 3 (depending on the year) was used to measure downwelling irradiance. Although the use of a dual spectrometer system may introduce some errors due to small spectral offsets even between spectrometers with the same specifications (Cendrero-Mateo et al., 2019), we chose this configuration in order to simultaneously measure sky and vegetation targets, thereby avoiding issues of differential illumination in sequential measurements. All spectrometers had an F-number of 4, a full width at half maximum of 0.45 μm, and used a #H36 grating, a 5 μm slit size, and 1044 pixel detectors. Table 1 summarizes the details of spectral range and resolution for each instrument.

2.3.1. Radiometric responsivity

The spectral radiance responsivity of each of our spectrometers was determined by transferring the scale of a calibrated Spectral Evolution SR3500 spectroradiometer using a large lamp-illuminated integrating sphere (diameter = 1.2 m with a 45 cm exit port). Radiometric responsivity values convert the raw digital number (DN) values recorded by the spectrometer detector into physical units of radiance (L) or irradiance (E). The fiber optic of the transfer spectroradiometer (TS) was mounted alongside the fiber and fore-optic of each instrument to be characterized, positioned so that the field of view was filled by the aperture of the integrating sphere.

In the case of the instrument used to measure radiance, the responsivity was calculated as in Eq. 1. The radiance-measuring spectrometer (RMS) was attached to an Ocean Insight QP400–2-VIS-NIR fiber optic cable; this cable was 2 m in length with a 400 μm core diameter. This fiber optic cable was coupled via a SubMiniature version A (SMA) connector to a 127 mm diameter reflector telescope with a focal length of 1250 mm (F/10). Radiometric responsivity was determined with this

Table 1

Spectrometer Specifications. Spectral range and resolution details for three grating spectrometers used in our analyses. Values in this table differ slightly from the nominal values specified by the manufacturer.

Instrument	Spectral range	Dispersion
QE Pro 1	650.2 nm to 883.6 nm	0.225 nm/pixel
QE Pro 2	650.3 nm to 878.6 nm	0.221 nm/pixel
QE Pro 3	650.2 nm to 876.5 nm	0.219 nm/pixel

telescope attached as in the field deployment. The telescope lens and calibrated spectroradiometer fiber tip were placed 49.5 cm from the integrating sphere aperture, a distance at which it was empirically determined that light from the integrating sphere filled the full field of view of the telescope.

$$Responsivity = (DN_{RMS} - DN_{RMS,dark})/L_{TS} \qquad (1)$$

Each spectrometer used to measure irradiance was deployed in the field and radiometrically calibrated with an Ocean Insight CC-3 cosine corrector attached via an SMA connector to an Ocean Insight custom fiber optic cable, 6.67 m in length with a 400 μm core diameter. To account for the diffusive properties of this cosine corrector, additional considerations were made during calibration design and responsivity calculation (SI Fig. 2). In order to avoid distance dependence issues when working with irradiance-measuring instruments, these measurements were made from a distance (D = 139.7 cm) at which the signal was empirically determined to plateau at equal or greater distances. To correct for the signal measured by the transfer spectroradiometer, which was not equipped with a cosine corrector, the aperture-fiber distance (D) and aperture area (A) were used to determine the solid angle (ω) being measured, and to convert the transfer spectroradiometer signal into irradiance values before calculating responsivity, as shown in Eqs. 2 to 4, where IMS is the irradiance-measuring spectrometer.

$$\omega = A/D^2 \qquad (2)$$

$$E_{TS} = L_{TS} \bullet \omega \qquad (3)$$

$$Responsivity = (DN_{IMS} - DN_{IMS,dark})/E_{TS} \qquad (4)$$

2.3.2. Laboratory signal-to-noise ratios

Multiple spectra ($n = 30$ for radiance-measuring spectrometer; $n = 5$ for irradiance-measuring spectrometers) were collected and averaged in order to determine radiometric responsivities from the large integrating sphere. Numbers of spectra were determined based on integration time needed to reach 80% to 90% of detector saturation, as well as the low variability in signal from the integrating sphere. The standard deviation between repeated measurements from the integrating sphere light source is approximately 5×10^{-5} W m^{-2} nm^{-1} sr^{-1}. Using these data, signal-to-noise ratios (SNR) were calculated by normalizing the mean of consecutively collected spectra by their standard deviation. Since the integrating sphere is a stable light source over the time of repeat spectrum collection, these represent SNR values under laboratory conditions with low humidity and stable temperature.

2.3.3. Fore-optics

Potential spectral effects of attached fore-optics were also tested by mounting spectrometers side by side on a balcony platform under clear sky conditions with all fore-optics removed. Spectra of sky illumination were recorded, then the same fiber was attached to each instrument one by one and the sky was re-measured. A cosine corrector was added to the end of the fiber following each measurement and sky illumination was again measured. All measurements for each instrument were made within 20 min of each other. No spectral shifts were observed as a result of attaching any fore-optics; more details and results of this test were described by Marrs et al. (2019).

2.3.4. Cosine corrector

A cosine corrector is a small disc of diffusive material added to the end of a fiber optic cable in order to reduce the angular effects of solar position when measuring downwelling irradiance in the field. While a perfect cosine corrector would collect light over a full 180°, allowing integrated measurements from the full hemisphere of the sky, imperfections in the diffusive disc or its housing would result in a more limited field of view and a potential underestimation of incoming irradiance. In order to characterize different diffusive materials used in the cosine

---

correctors being considered for our final field deployment, we tested the performance of three cosine correctors in a laboratory setting.

A spectrometer-coupled fiber optic cable was mounted on a rotating stage on one end of a laboratory optical bench. At the other end (distance = 232.4 cm), a 1000 W FEL lamp (Fraser et al., 2007) was mounted, centered in front of an alignment laser. A cosine corrector was connected to the front of the fiber optic cable, and a first measurement was made with the fiber aligned directly toward the FEL lamp, simulating a measurement with the sun directly overhead (simulated solar zenith angle = 0°). Measurements repeated at 10° increments away from the lamp in each direction, simulating solar zenith angles up to 60°. Photos of this experimental design can be found in SI Fig. 3. This procedure was performed using Ocean Insight CC-3 opal glass, Ocean Insight CC-3-UV-S Spectralon, and Ocean Insight CC-3-UV-T Teflon cosine correctors. The latter two materials are both made of polytetrafluoroethylene (PTFE); Teflon has a higher density and lower transmissivity than Spectralon (Tsai et al., 2008). In order to account for diffuse reflectance off other surfaces in the laboratory, a post (1.27 cm in diameter) was placed between the diffuser and FEL lamp, at a distance of 52.1 cm from the lamp. Black tape was added to the side of the post facing the diffuser in order to further reduce stray light reflected back in the direction of measurement. Measurements were repeated with the post in place with all diffuser materials at all angles, and the resulting diffuse signals were subtracted during analysis.

The performance of each diffusive material was characterized by comparing the amount of light collected at a simulated solar zenith angle of 0° to that collected at each angle away from center. With a perfect cosine corrector, the amount of measured light should fall off at extreme angles following a cosine function, where we would expect to see a 50% reduction in measured light intensity at 60° away from center. Reductions below this expected cosine curve in the laboratory translate to an underestimation of incoming irradiance in the field. This underestimation was calculated at multiple wavelengths in order to characterize spectral dependence in cosine correction. In order to characterize what these underestimations mean for SIF retrievals, custom R code (R Core Team, 2018) simulating solar geometry was written and run in RStudio (RStudio Team, 2015) to estimate resulting error at different times of day and year.

2.3.5. Electronic dark current

Detector electronic dark current was characterized in the laboratory by varying the integration time of measurements made while blocking light from the fiber port of each instrument. A linear function was fit to each set of measurements in order to describe the increase in dark current signal with increasing integration time. Data used to fit these linear functions were visualized by Marrs et al. (2019). During field measurements, these spectrometer-specific functions were used to subtract expected electronic dark current based on measurement integration time.

2.4. Field characterizations

At the FOREST field site, spectrometers were housed inside a temperature-controlled building (24 °C ± 2 °C) facing the FOREST treeline, with fiber optic cables running out through wall ports. The telescope used to measure reflected radiance from the treeline was situated on an external balcony, coupled to one of the fiber optic cables. The balcony extends from the third story of the field building, such that the treeline was viewed at a nearly perpendicular angle (SI Fig. 4). Although this view angle is more extreme than in some other tower systems, our meta-analysis revealed a wide range in view zenith angles in systems studied here (SI Fig. 5). When viewing over the approximately 100 m distance between balcony and treeline, the telescope field of view was approximately 0.75 m. Downwelling irradiance was measured using a fiber optic cable affixed along the external wall of the building, with the cosine corrector extending above the roof. For all field

data presented here, a cosine corrector with an opal glass diffuser was used.

2.4.1. Field signal-to-noise ratios

Signal-to-noise (SNR) values measured in the laboratory can provide an estimate of an instrument's performance when measuring a stable light source in controlled conditions. However, the SIF signal is faint and temporally dynamic, and must be retrieved from radiance and irradiance signals. SIF retrievals presented here were performed using the Fraunhofer Line Depth (FLD) method (Plascyk and Gabriel, 1975), in which SIF is retrieved as an in-filling in the atmospheric O_2-A absorption feature. This involves a transformation of spectral radiance and irradiance signals measured at 757.5 nm (λ_{out}) and 760.5 nm (λ_{in}); the full formula is presented in Eq. 5.

$$SIF = [(E_{\lambda out} \bullet L_{\lambda in}) - (L_{\lambda out} \bullet E_{\lambda in})]/(E_{\lambda out} - E_{\lambda in}) \tag{5}$$

Due to changes in solar position over hours and seasons, dynamic atmospheric conditions, and changes in leaf angle and illumination due to wind, we can expect both lower signal intensity and higher variability in the field than in the laboratory. In order to characterize these differences, SNRs were calculated from a time series of data collected continuously from 11:30 to 14:30 local time (15:30 to 18:30 GMT) on 6 September 2018 (day of year 249) for radiance and irradiance data at both in- and out-of-band wavelengths, as well as the resulting SIF retrievals. Each SNR time series was calculated as the mean of values recorded within a 5 min interval divided by the standard deviation of those values.

2.4.2. Atmospheric correction

Over the approximately 100 m path length between vegetation and balcony-mounted instrumentation (and even over much smaller distances), it is necessary to apply an atmospheric correction to recorded spectra in order to account for additional absorption by atmospheric O_2 along this 100 m path length. Atmospheric transmissivity at 760.5 nm (inside the well of the O_2-A absorption feature) was calculated as in Sabater et al. (2018) to account for atmospheric O_2 absorption, using air temperature, air pressure, and relative humidity data recorded as near as possible to the time of measurement. These values were also adjusted to the path length between the telescope and canopy area of interest, as determined using a TruPulse 200 hypsometer (Laser Technology, Inc., Centennial, CO, USA). The inverse of this transmissivity was then used to correct for the signal lost along the path from the treeline to the telescope.

2.5. Physiological measurements

Given the many above-described factors that affect field measurements of SIF, we performed a test to confirm that our deployed instrumentation could be used to measure a physiologically meaningful chlorophyll fluorescence signal. The Kautsky effect is a phenomenon in which photosystems of dark-acclimated vegetation suddenly exposed to light are temporarily unable to perform electron transfer, resulting in a large spike in fluorescence intensity as a compensatory mechanism, followed by a gradual decline upon the induction of photochemical and nonphotochemical mechanisms of chlorophyll de-excitation (Kautsky and Hirsch, 1931). This effect is traditionally measured using a pulse-amplitude modulated (PAM) fluorometer at the leaf level (Maxwell and Johnson, 2000), but can also be captured by remote observations.

A portion of *Quercus alba* (white oak) foliage, approximately 2 m in diameter and 100 m from the field building balcony, was dark-acclimated by covering with a tarp for 30 min. A FMSII PAM fluorometer (Hansatech Instruments Ltd., King's Lynn, Norfolk, UK), was attached to a healthy leaf on this branch just before removal of the tarp. The radiance-measuring telescope system was pointed at the center of this branch. Spectra were collected for 5 min, with a 5 s integration time determined based on illumination level. In this and all following field

experiments, integration time was set and dynamically adjusted with the goal of maintaining 80% to 90% of detector saturation.

2.6. Uncertainty estimation

Spectral measurements of downwelling irradiance and reflected radiance in the field are subject to angular, atmospheric, temporal, and illumination effects that may alter the final value of a SIF retrieval. We employed a Monte Carlo method to characterize the uncertainty resulting from these effects over the course of a day. For this estimation, we used idealized data for downwelling irradiance at both in-band ($E_{\lambda in}$) and out-of-band ($E_{\lambda out}$) wavelengths, and for out-of-band reflected radiance ($L_{\lambda out}$); these data were based on a smoothed time series of data collected at our field site (SI Fig. 6a-b). Smoothing was performed using the stat_smooth function in R (Wickham et al., 2019). We also used an idealized SIF time series for the same hours, based on SIF values retrieved from the original time series used to generate the smoothed radiance and irradiance data. For the purposes of this analysis, these values were considered to be true SIF magnitudes to which retrievals performed under different scenarios were compared. From these prescribed $E_{\lambda in}$, $E_{\lambda out}$, $L_{\lambda out}$, and SIF data, in-band radiance values ($L_{\lambda in}$) were calculated using the FLD SIF retrieval formula given in Eq. 5.

Using these values, we then performed a SIF observing system simulation experiment (OSSE), with different combinations of corrections for electronic dark current, detector noise, cosine corrector effects, and atmospheric O_2-A absorption applied during the retrieval process. The magnitude of the applied correction was calculated for each time point, depending on illumination level, solar geometry, and environmental parameters. The suncalc package in R (Thieurmel and Elmarhraoui, 2019) was used to determine solar geometry and was combined with the cosine corrector characterization data from Fig. 6 and SI Fig. 7 to account for cosine corrector error. A time series of air temperature, air pressure, and relative humidity were obtained from a nearby Weather Underground station (SI Fig. 6c-e) and were used as in Sabater et al. (2018) to calculate overall error in the atmospheric correction by adjusting the $L_{\lambda in}$ value from Eq. 5 to account for the estimated absorption along the path length between vegetation and sensor. This implementation applies to the standard FLD retrieval method, but atmospheric corrections must be calculated and implemented differently for other retrieval methods (Chang et al., 2020). In addition, distributions of uncertainty associated with each of these corrections were defined. Electronic dark correction and detector noise error distributions were determined from laboratory characterizations of three Ocean Insight QE Pro spectrometers; more details on these values can be found in Marrs et al. (2019). For each run of the OSSE simulation, dark current and detector noise effects were selected from known distributions. All errors were propagated through the SIF retrieval performed at each time point, producing a range of SIF values to be compared with the true SIF time series. For each combination of corrections, 500 simulations were performed. Table 2 shows details of the parameters and uncertainty distributions used in these simulations.

3. Results

In a meta-analysis of the literature on tower-based SIF-measuring systems, we found wide variability in reported SIF retrieval magnitudes, coupled with similar variation in instrumentation, hardware, and calibration methods. In order to contextualize this variability within the scope of field-deployed SIF-measuring systems, we characterized the performance of several spectrometers and associated hardware in both laboratory and field settings. We identified spectral, angular, and atmospheric effects with the potential to affect retrieved SIF values and to alter the performance of the field-deployed hardware below what laboratory characterizations would suggest. Based on variability in our hardware, we used a Monte Carlo approach to quantify the uncertainties in SIF retrievals introduced by several key corrections and calibrations.

Table 2
Parameters used in the observing system simulation.

Parameter	Value
Distance to target	100 m
Latitude	39.126° north
Longitude	77.221° west
Radiometric responsivity – radiance	In-band: 289.25 DN W^{-1} m^{-2} nm^{-1} sr^{-1} ms^{-1}
	Out-of-band: 291.5 DN W^{-1} m^{-2} nm^{-1} sr^{-1} ms^{-1}
Radiometric responsivity – irradiance	In-band: 242.3833 DN W^{-1} m^{-2} nm^{-1} ms^{-1}
	Out-of-band: 244.0667 DN W^{-1} m^{-2} nm^{-1} ms^{-1}
Air temperature uncertainty	Standard deviation = 0.3 °C
Air pressure uncertainty	Standard deviation = 50 mbar
Relative humidity uncertainty	Standard deviation = 5%
Dark correction distribution	Uniform distribution: Min = 0.015 ms DN^{-1} Max = 0.091 ms DN^{-1}
Detector noise distribution	Normal distribution: Mean = 0 DN, SD = 7.5 DN

Of these, the correction for atmospheric O_2 absorption in the wavelengths used for SIF retrievals showed the most dramatic effects; our meta-analysis showed that this correction is inconsistently applied in the literature. Overall, the results of our field testing suggest that differences in instrumentation and calibration across field studies may contribute to the wide variability in published SIF retrievals.

3.1. Meta-analysis

A meta-analysis of the literature on tower-based SIF measurements reveals a wide range in mean values for far-red SIF retrievals from unstressed vegetation. Discussion of the results and implications of this meta-analysis will focus on far-red SIF retrievals. Where available, mean and maximum SIF values from red wavelengths are summarized in SI Table 1 and show similar trends in mean SIF retrieval variability to far-red SIF retrievals. Although there is an established literature on the physiological information captured by different wavelengths of the chlorophyll emission spectrum (e.g. Magney et al., 2019b), we chose not to focus on red retrievals here, due to the smaller number of reported data in this wavelength range. Even within the red and far-red retrieval categories, differences exist among the various spectral windows or wavelengths used to perform SIF retrievals. A full analysis of these retrieval effects is outside the scope of this manuscript, but the choice of window size and central wavelength certainly also influences SIF magnitude (Cendrero-Mateo et al., 2019).

Although the majority of mean SIF values are below 4 mW m^{-2} nm^{-1} sr^{-1}, the full range of reported mean values spans three orders of magnitude, from 0.041 mW m^{-2} nm^{-1} sr^{-1} to 14.8 mW m^{-2} nm^{-1} sr^{-1} (Fig. 1a). Variability is also high even within seasons. Summer values for unstressed vegetation range two orders of magnitude, from 0.16 mW m^{-2} nm^{-1} sr^{-1} to 14.8 mW m^{-2} nm^{-1} sr^{-1} (Fig. 1b). These ranges include values across seasons; the minimum values from Magney et al. (2019a) are from a dataset collected on evergreens in winter, and the maximum value from Corp et al. (2006) are from an agricultural field in summer.

Within this wide variability, some patterns related to seasonality and land cover type emerge. SIF retrievals from forested targets show an annual pattern, with higher SIF values reported from spring and summer measurements than from autumn or winter measurements (Fig. 1b). Perhaps because of irrigation, multiple cropping cycles, fertilizer additions to croplands, and phenological or structural effects of different crops' growth phases, mean SIF values from agricultural areas do not show uniform spring and summer increases followed by declines in fall and winter. This difference may also have been driven by short agricultural growing seasons, which may not perfectly align with seasonal distinctions. Overall, SIF retrievals over agricultural lands are higher across all seasons, with a mean of 1.9 mW m^{-2} nm^{-1} sr^{-1} and a standard
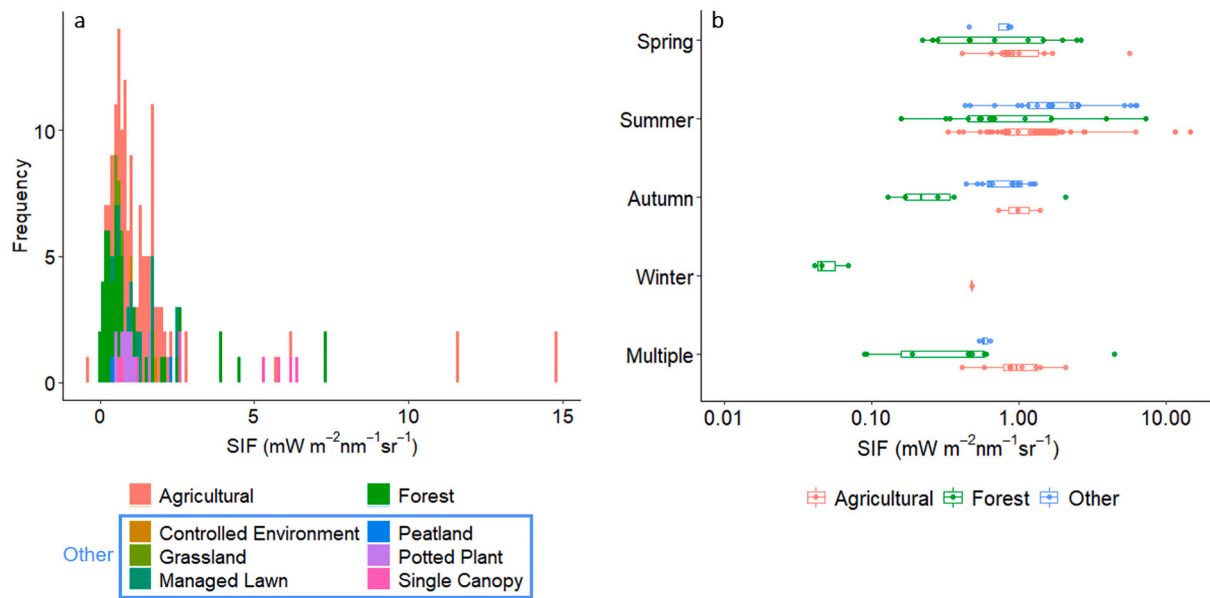
Fig. 1. Variability in SIF Retrievals from Literature Meta-Analysis. Published mean far-red SIF retrievals from unstressed vegetation, as a histogram color-coded by vegetation type (a) and seasonal boxplots color-coded by simplified vegetation type categories (b). In panel b, the x-axis is plotted on a log scale to illustrate the wide range of variability and enhance detail in boxplots. Boxes show 25th percentile, median, and 75th percentile with lines extending to 1.5 times the interquartile range. The "Multiple" category in panel b indicates values reported at a scale that averaged or aggregated observations across multiple seasons. (For interpretation of the references to color in this figure legend, the reader is referred to the web version of this article.)

error of ± 0.32 mW m^{-2} nm^{-1} sr^{-1}, as compared to 1.2 ± 0.25 mW m^{-2} nm^{-1} sr^{-1} in forests and 1.7 ± 0.25 mW m^{-2} nm^{-1} sr^{-1} across all other biomes.

In contrast to the strong SIF-GPP relationships observed at the satellite scale, mean SIF retrievals from tower and airborne relationships are not broadly predictive of the mean GPP values alongside which they were reported (Fig. 2). Linear models of the SIF-GPP relationship show small positive slopes in non-agricultural areas, but none of these slope coefficients are statistically significantly different from zero for any land cover type. Additionally, R^2 values of 0.0015 for agricultural areas, 0.03 for forests, and 0.23 for all other land covers show that mean SIF is not significantly correlated with mean GPP across the studies examined

here. It is worth noting that the mean values shown in Fig. 2 represent data collected from a variety of targets and locations with varied processing and averaging strategies, instrumentation, and calibration methodologies. SI Fig. 1b illustrates the number of corrections applied to the data shown in Fig. 2.

3.2. Calibrations and characterizations

Below, we describe several key sources of error in measuring spectra in laboratory and field settings, any of which may alter the final retrieved SIF signal. As a check on our system after calibration and corrections, we measured a Kautsky curve in order to confirm that physiologically meaningful signals matching leaf-level measurements could be recorded by our field instrumentation. The timing and relative magnitude of the SIF retrievals performed after exposing the dark-acclimated vegetation to light shows close agreement with steady-state fluorescence (F_s) measured at the leaf level, and indicate that our instrument deployment could capture the same fluorescence dynamics at a distance of 100 m as were seen with leaf-level instrumentation (see SI Fig. 4, Marrs et al., 2020).

One key challenge to reliable SIF measurements is the signal-to-noise ratio (SNR) of measurements of such a faint signal. In a laboratory setting, we found that, when measuring a stable light source (Fig. 3a) without any fore-optics attached to the fiber optic cable, the SNR was greater than 1000 over the majority of the spectral range of our spectrometers (Fig. 3b). The addition of the telescope decreased the SNR slightly, with a larger discrepancy observable in wavelengths >700 nm. The attachment of a cosine corrector resulted in a large loss of signal, approximately halving the SNR of the spectrometer across the spectral range as a result of the attenuated signal.

SNR values measured in field conditions are much more variable. Fig. 4a-b shows a time series of downwelling irradiance and reflected radiance measured continuously for three hours centered on solar noon (13:15 local time) on a day with intermittent cloud cover. Each panel shows radiance or irradiance measured both in and outside the O$_2$-A feature, wavelengths at which we expect to see very different signal magnitude due to atmospheric absorption effects. Fig. 4c-d shows these
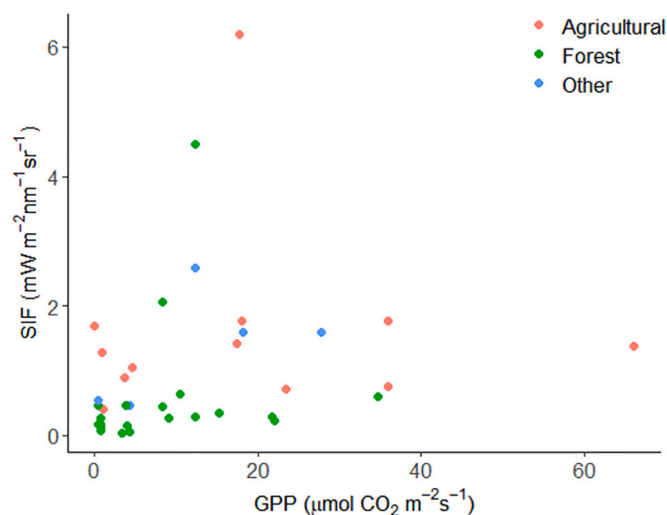

Fig. 2. SIF-GPP Relationships. Mean far-red SIF from unstressed vegetation plotted against mean GPP measured from the same vegetated target. Points are color-coded by simplified vegetation type, as in Fig. 1b. (For interpretation of the references to color in this figure legend, the reader is referred to the web version of this article.)
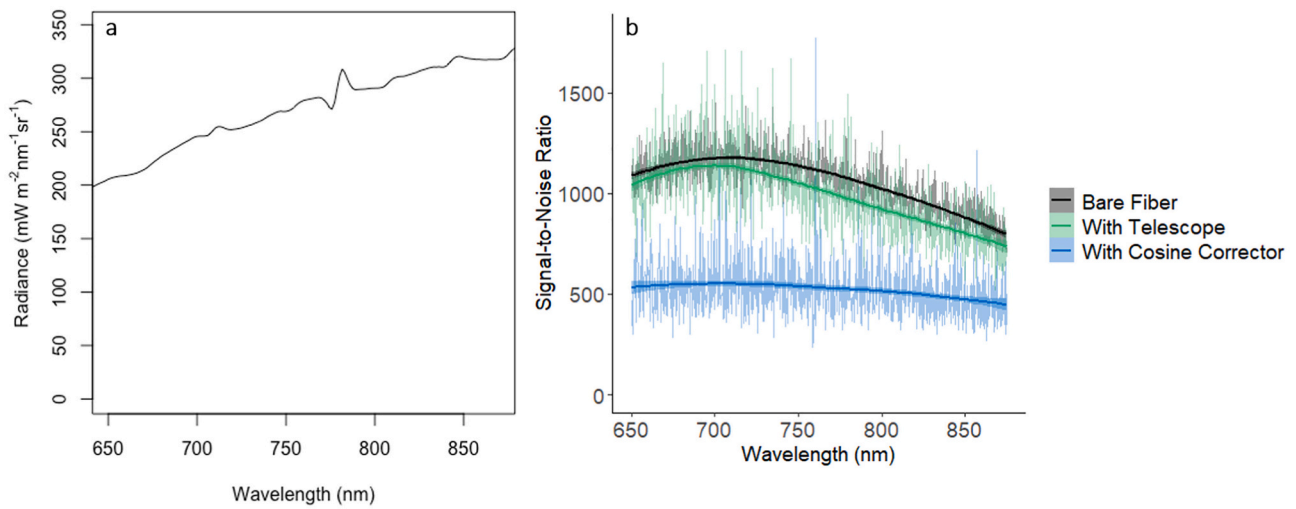
Fig. 3. Laboratory Signal-to-Noise Ratios. Signal-to-noise ratios calculated from repeated measurements of a known radiance source (a), using a bare fiber optic cable, as well as telescope and cosine corrector fore-optics (b). Error ranges around smoothed loess lines in panel b represent the 95% confidence interval.
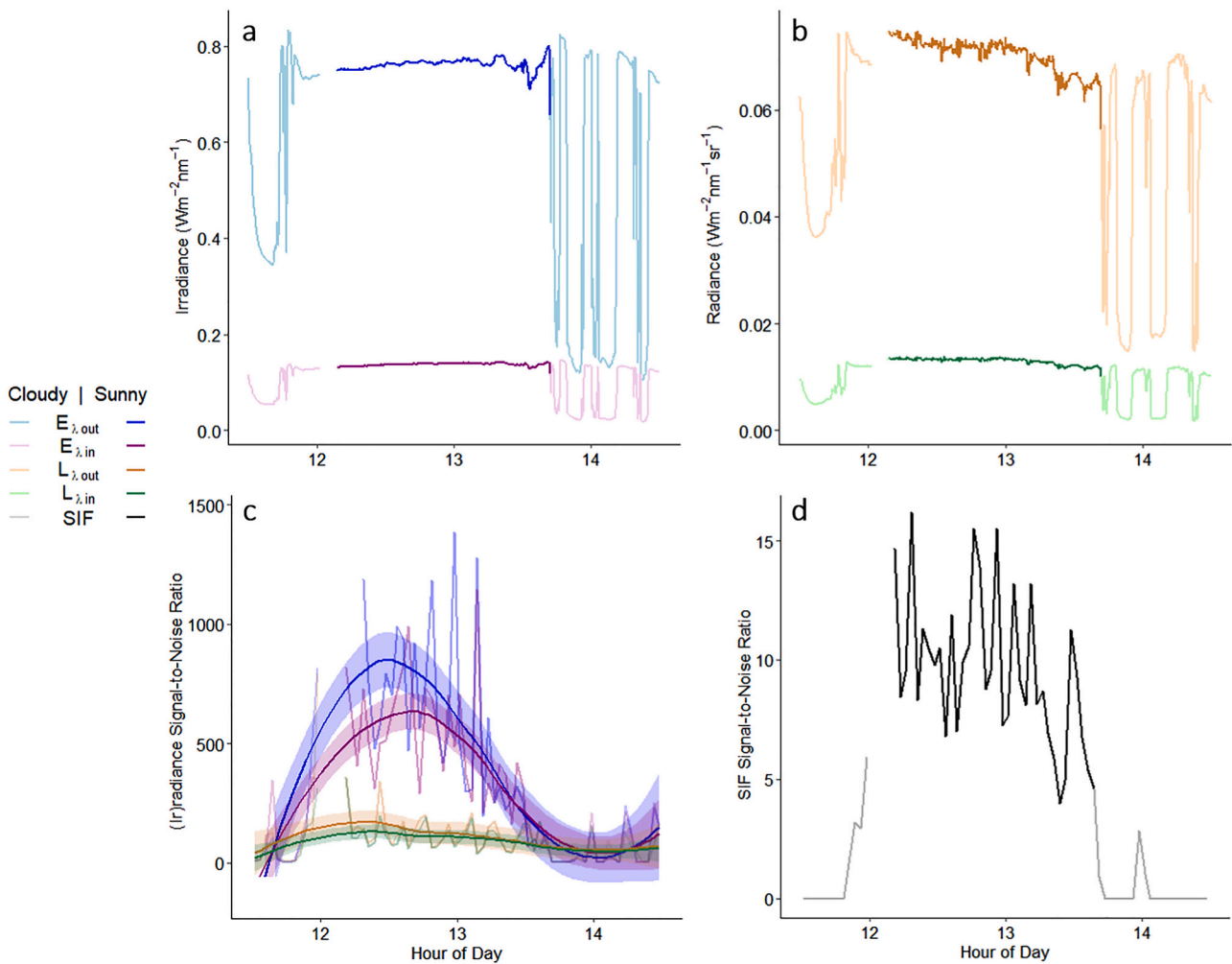

Fig. 4. Field Signal-to-Noise Ratios. Three hours of continuous in-band (λ_{in}) and out-of-band (λ_{out}) irradiance (E) and radiance (L) measurements collected in a field setting are shown in panels a and b. Signal-to-noise ratios were calculated from five-minute intervals of these data (c) and of the resulting SIF retrievals (d). Error ranges around smoothed loess lines in panel c represent the 95% confidence interval.

time series transformed into SNR values calculated at five-minute intervals. Irradiance measurements were collected every 1300 ms, so each SNR is calculated from the mean of 230 spectral irradiance values, divided by their standard deviation. Integration times for radiance reflected from relatively less bright treeline were 10 s, so 30 spectra are used to calculate each radiance SNR value. SIF retrievals are limited by the integration time of the radiance-measuring telescope system, so were also performed every 10 s and SNR was calculated as for radiance data.

During periods of clear skies, such as the period from approximately 12:10 to 13:40 local time shown in Fig. 4, irradiance SNR values are nearly as high as in the laboratory. Despite slight atmospheric variability during this period, signal intensity from the sun is nearly three times as bright as the integrating sphere light source. In contrast, the cloudy periods immediately preceding and following these clear skies result in much lower SNR values. Although irradiance intensities are occasionally as high as during the clear sky period, the greater signal variability results in a larger standard deviation over a five-minute interval and a decreased SNR. Although they were collected with the same spectrometer and telescope configuration tested in the laboratory, radiance SNR values in the field are much lower. This is driven by the lower reflectance from the vegetated target at which the telescope was aimed. In this

case, mean signal is low enough that overpassing clouds and resulting noise do not alter SNR values to the same degree seen with irradiance. All of this variability is commonplace in a field deployment, but is crucially important to retrieved SIF values. Over the course of this time series, the maximum SNR for five minutes of SIF retrievals was 16.2. These SNR values and those shown in Fig. 4 are particular to our system and the illumination levels measured during our laboratory and field tests. While exact SNR values may vary in other tower-based systems, these results highlight the additional errors introduced in field settings beyond those characterized in the laboratory.

Laboratory characterizations of diffusive materials used in fiber-coupled cosine correctors show all materials tested here lead to underestimations of incoming light (Fig. 5a). In our testing, opal glass outperformed either type of PTFE, but all materials show deviations from the theoretical cosine function expected in this kind of test. Discrepancies between expected and measured light intensities grow more extreme with simulated solar zenith angle (SZA), with errors of nearly 20% from measurements at a simulated solar zenith angle of 60° using a Teflon diffuser (Fig. 5b). Fig. 5c shows the course of SZA values throughout high light hours of the day on five days within the typical growing season in Maryland. On 6 September, the date on which the time series in Fig. 4 were collected, the highest SZA is 33.8°, with values
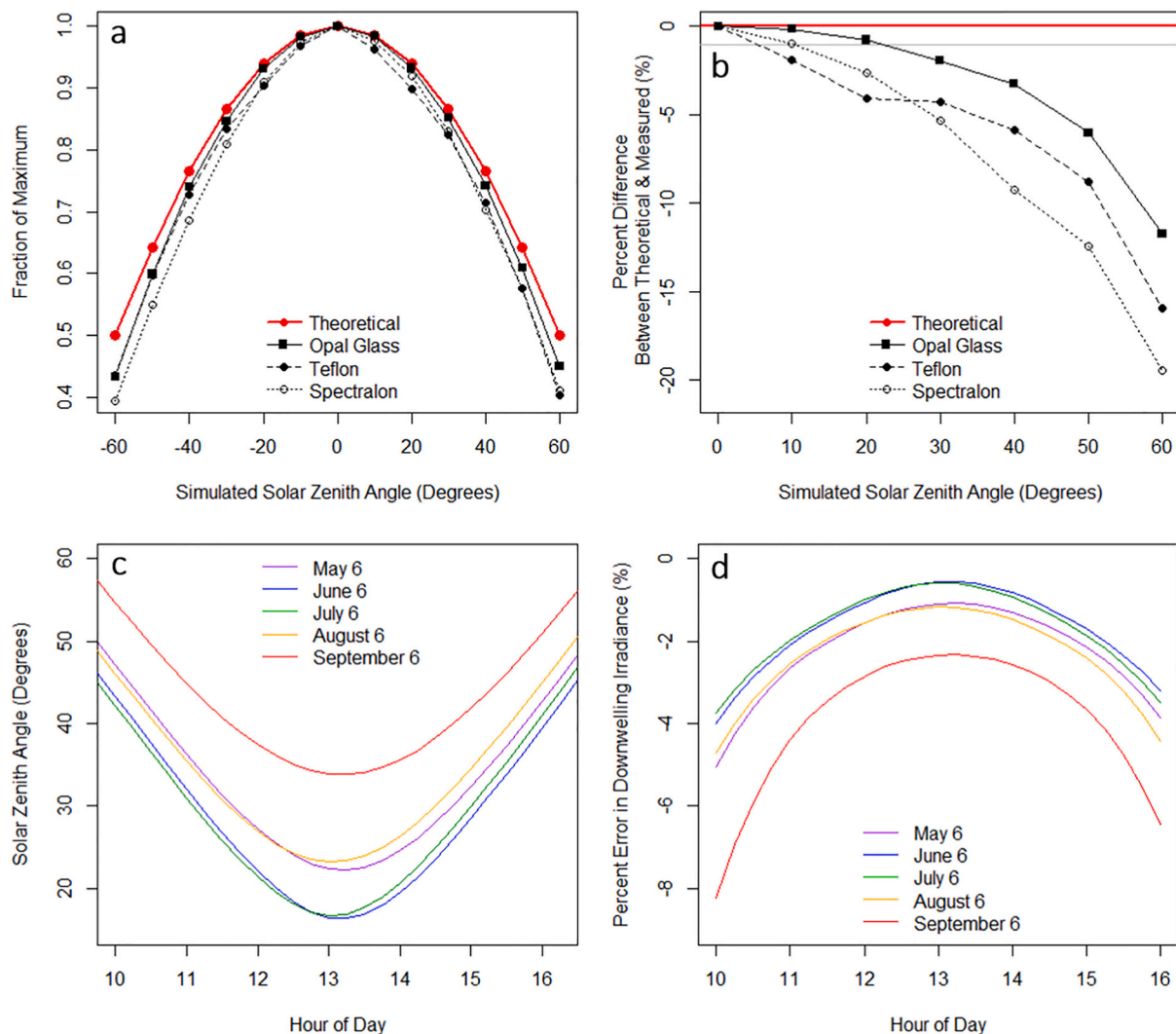

Fig. 5. Cosine corrector effects. Diffusive materials were characterized in terms of the fraction of the light from a 1000 W FEL lamp each captured at ten degree increments away from center (a) and as the percent deviation from the theoretical cosine function used to predict the decrease in signal intensity at more extreme angles (b). Simulated solar zenith angles in the laboratory are related to true solar geometry over a field site throughout the growing season (c) in order to predict percent error in measured downwelling solar irradiance across time of day and year (d).

up to 53.5° within three hours of solar noon. The use of an opal glass cosine corrector like the one deployed at our field site led to a 2% to 8% underestimation of downwelling solar irradiance, depending on the time of day (Fig. 5d). Across all materials tested here, these trends hold true across wavelengths; small variations in deviation from theoretical values were observed across the in-band and out-of-band wavelengths relevant to FLD SIF retrievals (SI Fig. 7). Measurements made at other times or days of year, or with other diffusive materials, will be associated with their own errors, which must be corrected in order to accurately quantify O_2-A in-filling and perform SIF retrievals.

3.3. Quantifying uncertainty in SIF retrievals

A simulation of the uncertainties introduced by performing the above-discussed corrections demonstrates that the magnitude of and variability in SIF retrievals is highly dependent on calibrations and corrections applied to measured spectra. Depending on the time of day, the magnitude of retrieved SIF values changes with illumination level, sun angle, and environmental parameters. These changes are represented as the offset between the true SIF time series shown in Fig. 7 and the solid lines corresponding to combinations of applied corrections and calibrations. The error ranges around these lines represent the uncertainties associated with the corrections themselves, as well as variability in detector noise. The size of each range is dependent on the error distribution and underlying assumptions used to generate it.

For example, the green line at the bottom of Fig. 6 represents a scenario in which all corrections have been applied, except for atmospheric O_2-A absorption. Failure to apply this correction dramatically changes retrieved SIF; values are negative at all hours of the day, due to absorption of all chlorophyll fluorescence and some reflected radiance by atmospheric O_2. For this simulation, we assume that spectra were collected by spectrometers whose electronic dark signal and cosine corrector effects are known and corrected. Since the atmospheric correction was not applied in this scenario, errors associated with temperature, pressure, and relative humidity measurements are not introduced to this calculation. Thus, the only remaining uncertainty around these SIF retrievals is the small effect of detector noise, resulting in the small error ribbon around this line. In contrast, the peach-colored line representing a simulation in which no corrections are applied has a much larger associated uncertainty. In this 'No Corrections' scenario, it is not assumed that we know and can correct for electronic dark signal and cosine corrector effects. Instead, values for these parameters are drawn from error distributions, leading to wider ranges of uncertainty in resulting SIF retrievals. In the scenario where dark, cosine, and atmospheric corrections have been applied, the uncertainty around SIF retrievals is largest at solar noon, with a standard deviation of approximately $\pm 6.6\%$ around retrieved SIF values. This value represents the uncertainty in our field measurement system after applying all corrections discussed above.

The atmospheric correction applied in Fig. 6 was calculated with the assumption of a 100 m distance between target and spectrometer (Table 2). However, the effects of atmospheric O_2 absorbance vary with path length, as well as with ambient temperature, relative humidity, and atmospheric pressure, as described in Sabater et al. (2018). Fig. 7 shows the distance-dependence of atmospheric corrections at constant environmental conditions. Values were calculated using atmospheric conditions measured as closely as possible to solar noon on 6 September 2018; air temperature was 32.8 °C with 53% relative humidity and 1.01 bars of atmospheric pressure. Along the 100 m from our telescope to the branch being measured at the treeline, approximately 9.5% of the signal inside the O_2-A feature is lost. Since this is the exact spectral window in which the FLD method measures in-filling from SIF emission, this is a crucial consideration. The rug plot at the base of the curve in Fig. 7 shows distances between instrumentation and target specified in papers in our meta-analysis. While some researchers are working at very short distances where atmospheric absorbance introduces very small errors, several papers describe SIF retrievals made from towers or small aircraft dozens or hundreds of meters from targeted vegetation, but do not discuss how this signal was corrected for atmospheric absorption along the path back to their instrumentation.

4. Discussion & conclusions

Intermediate-scale SIF retrievals performed on unstressed vegetation under high-light conditions span a wide range of magnitudes. We have documented differences in hardware specifications, calibration methodologies, vegetation type, and retrieval methods, as well as environmental parameters, that are major drivers of the variability in these
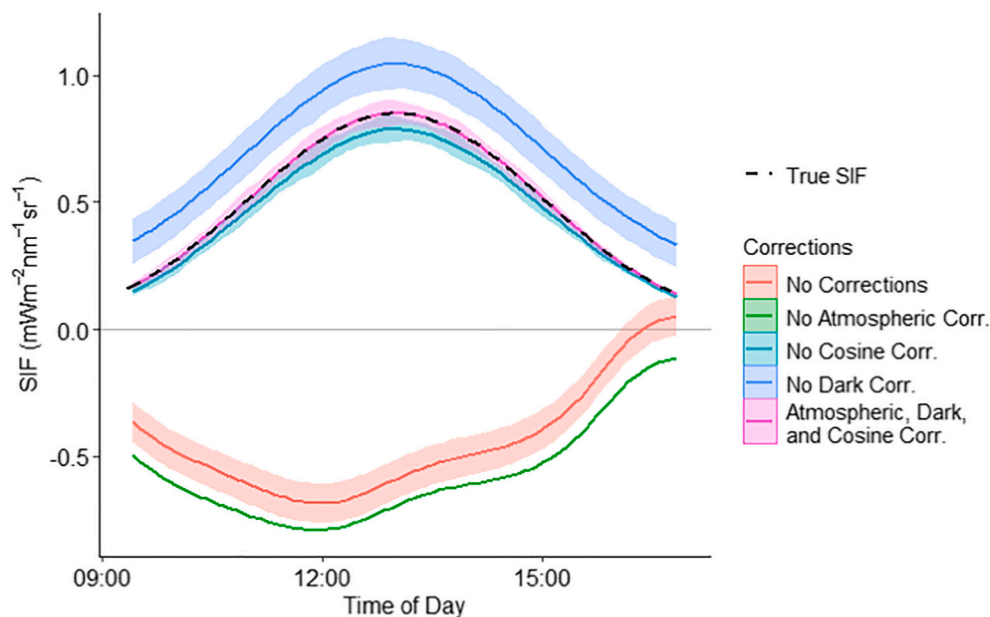
Fig. 6. Uncertainty Estimation. True SIF (dotted line) values from a Monte Carlo uncertainty estimation are compared to SIF retrievals performed after applying different combinations of corrections (colored lines) and the uncertainties around these retrievals (colored error ribbons). Error ribbons represent ± 1 standard deviation.
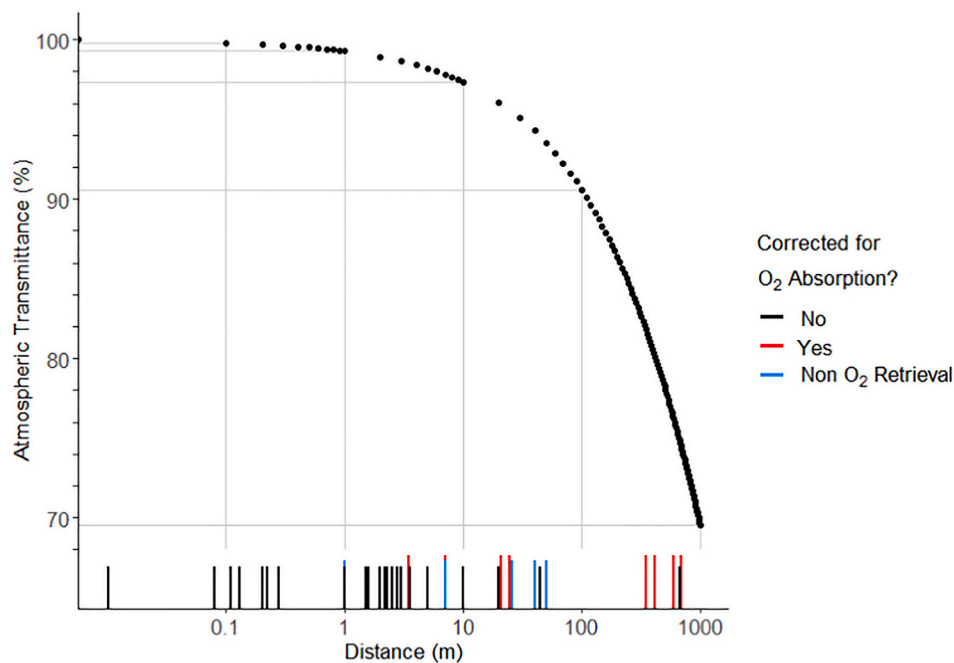
Fig. 7. Effects of Atmospheric O_2-A Absorption. Points represent the decline in atmospheric transmittance within the O_2-A feature as path length between sensor and target decreases, as predicted by calculations from Sabater et al. (2018). Rug plot represents distances at which field measurements were made, as reported in papers from a literature meta-analysis. Rug plot is color coded to differentiate cases in which measurements were or were not corrected for O_2 absorption effects, as well as cases where correction was unnecessary because of SIF retrievals performed outside O_2 absorption features.

published SIF values (SI Table 1). An OSSE simulation of uncertainties introduced by calibrations and corrections applied during SIF retrievals shows that SIF magnitudes, and the uncertainties around them, may vary widely depending on correction methodology. The impact of applying these corrections when making SIF retrievals in the field is dependent on careful site characterization in terms of sun-sensor-target geometry, atmospheric conditions, and environmental variability. Instrument and hardware specifications play a similarly important role and must be characterized in field conditions in order to account for limitations to the insight that laboratory characterizations can provide about sources of measurement noise under real-world conditions.

For example, we see that SNR varies dramatically based on sky conditions, sun angle, and target illumination. This mismatch is important beyond simply revealing that controlled laboratory experiments have limitations: the larger SNR values measured in the laboratory suggest that we may have more confidence in our ability to measure the SIF signal than is truly merited in the field. The Mission Advisory Group for the European Space Agency's FLuorescence EXplorer (FLEX) mission state in a recent report (Moreno et al., 2015) that SNR of at least 1015 in wavelengths outside the O_2-A feature, and 115 within it, is necessary to reliably measure a faint signal like SIF. Of the 61 papers examined in our meta-analysis, only seven discuss SNR values specific to different wavelengths and/or integration times, indicating that many systems may be limited by greater uncertainties in SIF retrievals than laboratory characterizations would suggest.

Accessory hardware and fore-optics, such as cosine correctors, are another often overlooked but crucial source of error in SIF retrievals. Underestimations of downwelling irradiance may not be obvious when making measurements in the field, but we show that significant discrepancies between true and measured irradiance may be introduced by cosine correctors, especially at more extreme sun angles. The magnitude of underestimation depends on the diffusive material, and its implications when making SIF retrievals depend on the retrieval method employed. In the case of the FLD SIF retrieval method, a single correction factor accounting for solar zenith angle would be applied in both the numerator and denominator. This factor would thus cancel out, resulting in the same SIF value as before the correction. Small differences in correction factors for in-band and out-of-band wavelengths (SI Fig. 4) are responsible for changes in retrieved SIF when using the FLD retrieval method. It should be noted that the results of our cosine corrector

characterizations capture only the effects of diffusive material under direct illumination. We did not attempt to characterize additional effects of diffuse light, although other ongoing research has examined this important consideration (e.g. Chang et al., 2020). Depending on the formulation of other retrieval methods, angle and wavelength dependence may affect final SIF retrievals to a greater or lesser degree. On the other hand, atmospheric O_2 absorption has a dramatic effect on measured SIF. Even the 100 m distance between our instrumentation and target introduced sufficient O_2 absorbance to mask all chlorophyll fluorescence emission before it reached the spectrometer. Both atmospheric and cosine corrector effects can be corrected post-measurement, but this requires careful characterization of sun-sensor-target geometry.

Broadly, our findings on the effects of hardware and instrumentation-associated uncertainties, namely those related to radiometric characterization and cosine corrector effects in a laboratory setting, are consistent with uncertainties modeled by Pacheco-Labrador et al. (2019). Our field results demonstrate that large errors can be introduced if atmospheric and angular corrections are not taken into account. It is likely that the varying implementation of these and other corrections across the published literature, along with differences in retrieval method, data filtering and averaging, and target type contribute to the wide range of published SIF values. Overall, the current SIF literature does not provide a clear consensus on SIF signal magnitudes or required instrument calibrations and corrections. Published SIF values vary beyond what might be expected from differences in species, season, or location. It is likely that the SIF instrumentation variability across the literature explains the lack of a strong relationship between mean SIF and mean GPP values at the tower scale. This finding stands in stark contrast to the close relationships observed at the satellite scale, where one set of carefully characterized instrumentation (per satellite platform) is used to make repeated measurements at a larger spatio-temporal scale that allows for linearization of the SIF-GPP relationship (Gu et al., 2019a). Nonetheless, more robust intermediate-scale SIF measurements are needed to make reliable inferences about photosynthetic rates or landscape-level primary productivity. Although important advances have been made in characterizing uncertainties within individual systems (Frankenberg et al., 2018; Grossmann et al., 2018; Gu et al., 2019b; Pacheco-Labrador et al., 2019), improvements are still needed, for example in developing improved atmospheric corrections for tower-based SIF retrievals. In the next steps of our work, we plan to

continue characterizing stray light effects, following the methods described by Zong et al. (2006), as well as detector nonlinearity and temperature and humidity effects. Perhaps because of the difficulty of making such measurements, these are among the more frequently neglected corrections in the literature. In summary, there is a crucial need for best practice guidelines for characterization of spectrometers, hardware, and site characteristics in airborne and tower-based systems. Improving the reliability of intermediate-scale measurements will increase the utility of SIF as a parameter in models of primary productivity and help to further our understanding of methodologies to remotely monitor plant physiology.

Declaration of Competing Interest

The authors declare that they have no known competing financial interests or personal relationships that could have appeared to influence the work reported in this paper.

Acknowlegements

Appendix A. Supplementary data

Supplementary data to this article can be found online at https://doi.org/10.1016/j.rse.2021.112413.

References

Albert, L., Cushman, K.C., Allen, D.W., Zong, Y., Alonso, L., Kellner, J.R., 2019. Stray light characterization in a high-resolution imaging spectrometer designed for solar-induced fluorescence. In: Proceedings of SPIE 10986, Algorithms, Technologies, and Applications for Multispectral and Hyperspectral Imagery, XXV, p. 15. https://doi.org/10.1117/12.2519395.

Anav, A., Friedlingstein, P., Beer, C., Ciais, P., Harper, A., Jones, C., Murray-Tortarolo, G., Papale, D., Parazoo, N.C., Peylin, P., Piao, S., Sitch, S., Viovy, N., Wiltshire, A., Zhao, M., 2015. Spatiotemporal patterns of terrestrial gross primary production: a review. Rev. Geophys. 53, 785–817. https://doi.org/10.1002/2015RG000483.

Asner, G.P., Nepstad, D., Cardinot, G., Ray, D., 2004. Drought stress and carbon uptake in an Amazon forest measured with spaceborne imaging spectroscopy. Proc. Natl. Acad. Sci. 101, 6039–6044. https://doi.org/10.1073/pnas.0400168101.

Baker, N.R., 2008. Chlorophyll fluorescence: a probe of photosynthesis in vivo. Annu. Rev. Plant Biol. 59, 89–113. https://doi.org/10.1146/annurev.arplant.59.032607.092759.

Burkart, A., Schickling, A., Mateo, M.P.C., Wrobel, T.J., Rossini, M., Cogliati, S., Julitta, T., Rascher, U., 2015. A method for uncertainty assessment of passive sun-induced chlorophyll fluorescence retrieval using an infrared reference light. IEEE Sensors J. 15, 4603–4611. https://doi.org/10.1109/JSEN.2015.2422894.

Campbell, P.K.E., Huemmrich, K.F., Middleton, E.M., Ward, L.A., Julitta, T., Daughtry, C.S.T., Burkart, A., Russ, A.L., Kustas, W.P., 2019. Diurnal and seasonal variations in chlorophyll fluorescence associated with photosynthesis at leaf and canopy scales. Remote Sens. 11, 1–27. https://doi.org/10.3390/rs11050488.

Cendrero-Mateo, M.P., Wieneke, S., Damm, A., Alonso, L., Pinto, F., Moreno, J., Guanter, L., Celesti, M., Rossini, M., Sabater, N., Cogliati, S., Julitta, T., Rascher, U., Goulas, Y., Aasen, H., Pacheco-Labrador, J., Mac Arthur, A., 2019. Sun-induced chlorophyll fluorescence III: benchmarking retrieval methods and sensor characteristics for proximal sensing. Remote Sens. 11, 1–28. https://doi.org/10.3390/rs11080962.

Chang, C.Y., Guanter, L., Frankenberg, C., Köhler, P., Gu, L., Magney, T.S., Grossmann, K., Sun, Y., 2020. Systematic assessment of retrieval methods for canopy far-red solar-induced chlorophyll fluorescence using high-frequency automated field spectroscopy. J. Geophys. Res. Biogeosci. 125, 1–26. https://doi.org/10.1029/2019JG005533.

Corp, L.A., Middleton, E.M., Daughtry, C.S.T., Campbell, P.K.E., 2006. Solar induced fluorescence and reflectance sensing techniques for monitoring nitrogen utilization in corn. In: International Geoscience and Remote Sensing Symposium (IGARSS), pp. 2267–2270. https://doi.org/10.1109/IGARSS.2006.586.

Dechant, B., Ryu, Y., Badgley, G., Zeng, Y., Berry, J.A., Zhang, Y., Goulas, Y., Li, Z., Zhang, Q., Kang, M., Li, J., Moya, I., 2020. Canopy structure explains the relationship between photosynthesis and sun-induced chlorophyll fluorescence in crops. Remote Sens. Environ. 241. https://doi.org/10.1016/j.rse.2020.111733.

Duveiller, G., Cescatti, A., 2016. Spatially downscaling sun-induced chlorophyll fluorescence leads to an improved temporal correlation with gross primary productivity. Remote Sens. Environ. 182, 72–89. https://doi.org/10.1016/j.rse.2016.04.027.

Frankenberg, C., Fisher, J.B., Worden, J., Badgley, G., Saatchi, S.S., Lee, J.E., Toon, G.C., Butz, A., Jung, M., Kuze, A., Yokota, T., 2011. New global observations of the terrestrial carbon cycle from GOSAT: patterns of plant fluorescence with gross primary productivity. Geophys. Res. Lett. https://doi.org/10.1029/2011GL048738.

Frankenberg, C., Kohler, P., Magney, T.S., Geier, S., Lawson, P., Schwochert, M., McDuffie, J., Drewry, D.T., Pavlick, R., Kuhnert, A., 2018. The Chlorophyll Fluorescence Imaging Spectrometer (CFIS), mapping far red fluorescence from aircraft. Remote Sens. Environ. 217, 523–536. https://doi.org/10.1016/j.rse.2018.08.032.

Fraser, G.T., Gibson, C.E., Yoon, H.W., Parr, A.C., 2007. "Once is enough" in radiometric calibrations. J. Res. Natl. Inst. Stand. Technol. 112, 39–51. https://doi.org/10.6028/jres.112.003.

Goulas, Y., Fournier, A., Daumard, F., Champagne, S., Ounis, A., Marloie, O., Moya, I., 2017. Gross primary production of a wheat canopy relates stronger to far red than to red solar-induced chlorophyll fluorescence. Remote Sens. 9, 1–31. https://doi.org/10.3390/rs9010097.

Grossmann, K., Frankenberg, C., Magney, T.S., Hurlock, S.C., Seibt, U., Stutz, J., 2018. PhotoSpec: a new instrument to measure spatially distributed red and far-red solar-induced chlorophyll fluorescence. Remote Sens. Environ. 216, 311–327. https://doi.org/10.1016/j.rse.2018.07.002.

Gu, L., Han, J., Wood, J.D., Chang, C.Y.Y., Sun, Y., 2019a. Sun-induced Chl fluorescence and its importance for biophysical modeling of photosynthesis based on light reactions. New Phytol. 223, 1179–1191. https://doi.org/10.1111/nph.15796.

Gu, L., Wood, J.D., Chang, C.Y.Y., Sun, Y., Riggs, J.S., 2019b. Advancing terrestrial ecosystem science with a novel automated measurement system for sun-induced chlorophyll fluorescence for integration with Eddy covariance flux networks. J. Geophys. Res. Biogeosci. 124, 127–146. https://doi.org/10.1029/2018JG004742.

Huwaldt, J.A., 2015. Plot Digitizer [WWW Document]. URL. plotdigitizer.sourceforge.net.

Julitta, T., Corp, L.A., Rossini, M., Burkart, A., Cogliati, S., Davies, N., Hom, M., Arthur, A. Mac, Middleton, E.M., Rascher, U., Schickling, A., Colombo, R., 2016. Comparison of sun-induced chlorophyll fluorescence estimates obtained from four portable field spectroradiometers. Remote Sens. 8, 1–14. https://doi.org/10.3390/rs8020122.

Kautsky, H., Hirsch, A., 1931. Neue Versuche zur Kohlensäureassimilation. Naturwissenschaften 19, 964.

Krause, G.H., Weis, E., 1991. Chlorophyll fluorescence and photosynthesis: the basics. Annu. Rev. Plant Physiol. Plant Mol. Biol. 42, 313–349. https://doi.org/10.1002/9780470122563.ch3.

Le Quéré, C., Andrew, R.M., Friedlingstein, P., Sitch, S., Pongratz, J., Manning, A.C., Korsbakken, J.I., Peters, G.P., Canadell, J.G., Jackson, R.B., Boden, T.A., Tans, P.P., Andrews, O.D., Arora, V.K., Bakker, D.C.E., Barbero, L., Becker, M., Betts, R.A., Bopp, L., Chevallier, F., Chini, L.P., Ciais, P., Cosca, C.E., Cross, J., Currie, K., Gasser, T., Harris, I., Hauck, J., Haverd, V., Houghton, R.A., Hunt, C.W., Hurtt, G., Ilyina, T., Jain, A.K., Kato, E., Kautz, M., Keeling, R.F., Klein Goldewijk, K., Körtzinger, A., Landschützer, P., Lefèvre, N., Lenton, A., Lienert, S., Lima, I., Lombardozzi, D., Metzl, N., Millero, F., Monteiro, P.M.S., Munro, D.R., Nabel, J.E.M.S., Nakaoka, S.-I., Nojiri, Y., Padin, X.A., Peregon, A., Pfeil, B., Pierrot, D., Poulter, B., Rehder, G., Reimer, J., Rödenbeck, C., Schwinger, J., Séférian, R., Skjelvan, I., Stocker, B.D., Tian, H., Tilbrook, B., Tubiello, F.N., Van Der Laan-Luijkx, I.T., Van Der Werf, G.R., Van Heuven, S., Viovy, N., Vuichard, N., Walker, A.P., Watson, A.J., Wiltshire, A.J., Zaehle, S., Zhu, D., 2018. Global carbon budget 2017. Earth Syst. Sci. Data 10, 405–448. https://doi.org/10.5194/essd-10-405-2018.

Li, L., Dai, C., Wu, Z., Wang, Y., 2018a. Temperature correction method for commercial CCD array spectrometers used in spectral radiometry measurement. J. Phys. Conf. Ser. 972, 0–6. https://doi.org/10.1088/1742-6596/972/1/012020.

Li, X., Xiao, J., He, B., 2018b. Chlorophyll fluorescence observed by OCO-2 is strongly related to gross primary productivity estimated from flux towers in temperate forests. Remote Sens. Environ. 204, 659–671. https://doi.org/10.1016/j.rse.2017.09.034.

Lin, X., Chen, B., Zhang, H., Wang, F., Chen, J., Guo, L., Kong, Y., 2019. Effects of the temporal aggregation and meteorological conditions on the parameter robustness of OCO-2 SIF-based and LUE-based GPP models for croplands. Remote Sens. 11 https://doi.org/10.3390/rs11111328.

Liu, L., Liu, X., Hu, J., Guan, L., 2017. Assessing the wavelength-dependent ability of solar-induced chlorophyll fluorescence to estimate the GPP of winter wheat at the canopy level. Int. J. Remote Sens. 38, 4396–4417. https://doi.org/10.1080/01431161.2017.1320449.

Magney, T.S., Bowling, D.R., Logan, B.A., Grossmann, K., Stutz, J., Blanken, P.D., Burns, S.P., Cheng, R., Garcia, M.A., Kohler, P., Lopez, S., Parazoo, N.C., Raczka, B., Schimel, D., Frankenberg, C., 2019a. Mechanistic evidence for tracking the seasonality of photosynthesis with solar-induced fluorescence. Proc. Natl. Acad. Sci. U. S. A. 116, 11640–11645. https://doi.org/10.1073/pnas.1900278116.

Magney, T.S., Frankenberg, C., Kohler, P., North, G., Davis, T.S., Dold, C., Dutta, D., Fisher, J.B., Grossmann, K., Harrington, A., Hatfield, J., Stutz, J., Sun, Y., Porcar-Castell, A., 2019b. Disentangling changes in the spectral shape of chlorophyll fluorescence: implications for remote sensing of photosynthesis. J. Geophys. Res. Biogeosci. 124, 1491–1507. https://doi.org/10.1029/2019JG005029.

Magney, T.S., Barnes, M.L., Yang, X., 2020. On the covariation of chlorophyll fluorescence and photosynthesis across scales. Geophys. Res. Lett. 47, 1–7. https://doi.org/10.1029/2020GL091098.

Marrs, J.K., Hutyra, L.R., Allen, D.W., 2019. Solar-induced fluorescence retrievals in the context of physiological, environmental, and hardware-based sources of uncertainty. In: Proceedings of SPIE 10986, Algorithms, Technologies, and Applications for Multispectral and Hyperspectral Imagery, XXV, pp. 1–14. https://doi.org/10.1117/12.2520457.

Marrs, J.K., Reblin, J.S., Logan, B.A., Allen, D.W., Reinmann, A.B., Bombard, D.M., Tabachnik, D., Hutyra, L.R., 2020. Solar-induced fluorescence does not track photosynthetic carbon assimilation following induced stomatal closure. Geophys. Res. Lett. 47, 1–11. https://doi.org/10.1029/2020GL087956.

Maxwell, K., Johnson, G.N., 2000. Chlorophyll fluorescence—a practical guide. J. Exp. Bot. 51, 659–668. https://doi.org/10.1093/jxb/51.345.659.

Meroni, M., Rossini, M., Guanter, L., Alonso, L., Rascher, U., Colombo, R., Moreno, J., 2009. Remote sensing of solar-induced chlorophyll fluorescence: review of methods and applications. Remote Sens. Environ. https://doi.org/10.1016/j.rse.2009.05.003.

Middleton, E.M., Rascher, U., Corp, L.A., Huemmrich, K.F., Cook, B.D., Noormets, A., Schickling, A., Pinto, F., Alonso, L., Damm, A., Guanter, L., Colombo, R., Campbell, P.K.E., Landis, D.R., Zhang, Q., Rossini, M., Schuettemeyer, D., Bianchi, R., 2017. The 2013 FLEX-US airborne campaign at the parker tract loblolly pine plantation in North Carolina, USA. Remote Sens. 9, 1–31. https://doi.org/10.3390/rs9060612.

Migliavacca, M., Perez-Priego, O., Rossini, M., El-Madany, T.S., Moreno, G., van der Tol, C., Rascher, U., Berninger, A., Bessenbacher, V., Burkart, A., Carrara, A., Fava, F., Guan, J.-H., Hammer, T.W., Henkel, K., Juarez-Alcalde, E., Julitta, T., Kolle, O., Pilar Martin, M., Musavi, T., Pacheco-Labrador, J., Perez-Burgueno, A., Wutzler, T., Zaehle, S., Reichstein, M., 2017. Plant functional traits and canopy structure control the relationship between photosynthetic CO2 uptake and far-red sun-induced fluorescence in a Mediterranean grassland under different nutrient availability. New Phytol. 214, 1078–1091. https://doi.org/10.1111/nph.14437.

Moreno, J., Goulas, Y., Huth, A., Middleton, E., Miglietta, F., Mohammed, G., Nedbal, L., Rascher, U., Verhoef, W., 2015. Report for Mission Selection: FLEX (ESA SP-1330/2, June 2015), Noordwijk, Netherlands.

Nichol, C.J., Drolet, G., Porcar-Castell, A., Wade, T., Sabater, N., Middleton, E.M., MacLellan, C., Levula, J., Mammarella, I., Vesala, T., Atherton, J., 2019. Diurnal and seasonal solar induced chlorophyll fluorescence and photosynthesis in a boreal scots pine canopy. Remote Sens. 11, 1–22. https://doi.org/10.3390/rs11030273.

Pacheco-Labrador, Hueni, Mihai, Sakowska, Julitta, Kuusk, Sporea, Alonso, Burkart, Cendrero-Mateo, Aasen, Goulas, Arthur, Mac, 2019. Sun-induced chlorophyll fluorescence I: instrumental considerations for proximal spectroradiometers. Remote Sens. 11, 1–30. https://doi.org/10.3390/rs11080960.

Pan, Y., Birdsey, R.A., Fang, J., Houghton, R., Kauppi, P.E., Kurz, W.A., Phillips, O.L., Shvidenko, A., Lewis, S.L., Canadell, J.G., Ciais, P., Jackson, R.B., Pacala, S.A., McGuire, D., Piao, Shilong, Rautiainen, A., Sitch, S., Hayes, D., 2011. A large and persistent carbon sink in the world's forests. Science (80-.) 333, 988–993. https://doi.org/10.1126/science.1201609.

Plascyk, J.A., Gabriel, F.C., 1975. The Fraunhofer line discriminator MKII-an airborne instrument for precise and standardized ecological luminescence measurement. IEEE Trans. Instrum. Meas. 24, 306–313. https://doi.org/10.1109/TIM.1975.4314448.

Porcar-Castell, A., Tyystjärvi, E., Atherton, J., Van Der Tol, C., Flexas, J., Pfündel, E.E., Moreno, J., Frankenberg, C., Berry, J.A., 2014. Linking chlorophyll a fluorescence to photosynthesis for remote sensing applications: mechanisms and challenges. J. Exp. Bot. 65, 4065–4095. https://doi.org/10.1093/jxb/eru191.

R Core Team, 2018. R: A Language and Environment for Statistical Computing. R Foundation for Statistical Computing.

RStudio Team, 2015. RStudio: Integrated Development for R.

Ryu, Y., Berry, J.A., Baldocchi, D.D., 2019. What is global photosynthesis? History, uncertainties and opportunities. Remote Sens. Environ. 223, 95–114. https://doi.org/10.1016/j.rse.2019.01.016.

Sabater, N., Vicent, J., Alonso, L., Verrelst, J., Middleton, E.M., Porcar-Castell, A., Moreno, J., 2018. Compensation of oxygen transmittance effects for proximal sensing retrieval of canopy-leaving sun-induced chlorophyll fluorescence. Remote Sens. 10, 1–29. https://doi.org/10.3390/rs10101551.

Smith, I.A., Hutyra, L.R., Reinmann, A.B., Thompson, J.R., Allen, D.W., 2019. Evidence for edge enhancements of soil respiration in temperate forests. Geophys. Res. Lett. 46, 4278–4287. https://doi.org/10.1029/2019GL082459.

Sun, Y., Frankenberg, C., Jung, M., Joiner, J., Guanter, L., Köhler, P., Magney, T., 2018. Overview of solar-induced chlorophyll fluorescence (SIF) from the orbiting carbon observatory-2: retrieval, cross-mission comparison, and global monitoring for GPP. Remote Sens. Environ. 209, 808–823. https://doi.org/10.1016/j.rse.2018.02.016.

Thieurmel, B., Elmarhraoui, A., 2019. suncalc.

Thompson, S.D., Nelson, T.A., Coops, N.C., Wulder, M.A., Lantz, T.C., 2017. Global spatial–temporal variability in terrestrial productivity and phenology regimes between 2000 and 2012. Ann. Am. Assoc. Geogr. 107, 1519–1537. https://doi.org/10.1080/24694452.2017.1309964.

Tsai, B.K., Allen, D.W., Hanssen, L.M., Wilthan, B., Zeng, J., 2008. A Comparison of Optical Properties between High Density and Low Density Sintered PTFE. Reflection, Scatt. Diffr. from Surfaces, 70650Y, pp. 1–9. https://doi.org/10.1117/12.798138.

Verma, M., Schimel, D., Evans, B., Frankenberg, C., Beringer, J., Drewry, D.T., Magney, T., Marang, I., Hutley, L., Moore, C., Eldering, A., 2017. Effect of environmental conditions on the relationship between solar-induced fluorescence and gross primary productivity at an OzFlux grassland site. J. Geophys. Res. Biogeosci. 122, 716–733. https://doi.org/10.1002/2016JG003580.

Wickham, H., Averick, M., Bryan, J., Chang, W., McGowan, L.D., François, R., Grolemund, G., Hayes, A., Henry, L., Hester, J., Kuhn, M., Pederson, T.L., Miller, E., Bache, S.M., Müller, K., Ooms, J., Robinson, D., Seidel, D.P., Spinu, V., Takahashi, K., Vaughan, D., Wilke, C., Woo, K., Yutani, H., 2019. Welcome to the tidyverse. J. Open Source Softw. 4, 1–1686.

Wieneke, S., Burkart, A., Cendrero-Mateo, M.P., Julitta, T., Rossini, M., Schickling, A., Schmidt, M., Rascher, U., 2018. Linking photosynthesis and sun-induced fluorescence at sub-daily to seasonal scales. Remote Sens. Environ. 219, 247–258. https://doi.org/10.1016/j.rse.2018.10.019.

Wood, J.D., Griffis, T.J., Baker, J.M., Frankenberg, C., Verma, M., Yuen, K., 2017. Multiscale analyses of solar-induced florescence and gross primary production. Geophys. Res. Lett. 44, 533–541. https://doi.org/10.1002/2016GL070775.

Xiao, J., Li, X., He, B., Arain, M.A., Beringer, J., Desai, A.R., Emmel, C., Hollinger, D.Y., Krasnova, A., Mammarella, I., Noe, S.M., Serrano Ortiz, P., Rey-Sanchez, C., Rocha, A.V., Varlagin, A., 2019. Solar-induced chlorophyll fluorescence exhibits a universal relationship with gross primary productivity across a wide variety of biomes. Glob. Chang. Biol. 1–4 https://doi.org/10.1111/gcb.14565.

Yang, H., Yang, X., Zhang, Y., Heskel, M.A., Lu, X., Munger, J.W., Sun, S., Tang, J., 2017. Chlorophyll fluorescence tracks seasonal variations of photosynthesis from leaf to canopy in a temperate forest. Glob. Chang. Biol. 23, 2874–2886. https://doi.org/10.1111/gcb.13590.

Zarco-Tejada, P.J., Gonzalez-Dugo, M.V., Fereres, E., 2016. Seasonal stability of chlorophyll fluorescence quantified from airborne hyperspectral imagery as an indicator of net photosynthesis in the context of precision agriculture. Remote Sens. Environ. 179, 89–103. https://doi.org/10.1016/j.rse.2016.03.024.

Zhang, Z., Zhang, Y., Joiner, J., Migliavacca, M., 2018. Angle matters: bidirectional effects impact the slope of relationship between gross primary productivity and sun-induced chlorophyll fluorescence from Orbiting Carbon Observatory-2 across biomes. Glob. Chang. Biol. 1–4 https://doi.org/10.1111/gcb.14427.

Zong, Y., Brown, S.W., Johnson, B.C., Lykke, K.R., Ohno, Y., 2006. Simple spectral stray light correction method for array spectroradiometers. Appl. Opt. 45, 1111–1119. https://doi.org/10.1364/AO.45.001111.